TEC and Ionospheric Height Estimation by Means of Azimuth Subaperture Analysis in Quad-Polarimetric Spaceborne SAR Data

Jun Su Kim and Konstantinos P. Papathanassiou, *Fellow, IEEE*

***Abstract*—The total electron content (TEC) is probably the most important single parameter to characterize the ionospheric state and its impact on synthetic aperture radar (SAR) data. Its accurate estimation is therefore essential when it comes to the correction and calibration of SAR data distorted by the ionosphere. In recent years, the estimation of Faraday rotation (FR), i.e., the rotation of the polarimetric plane of the transmitted and scattered EM pulses as they propagate through the ionosphere, has become a key element of TEC estimation. FR is proportional to TEC and to the line-of-sight (LOS) component of the geomagnetic field. The availability of quad-polarimetric SAR data allows the precise estimation of FR, and thus TEC. However, an accurate TEC estimation requires knowledge of the geomagnetic field that varies with height. In this sense, the knowledge of the ionospheric height becomes an important issue for a correct FR to TEC conversion. While the estimation performance of FR is well understood, our understanding of the ionospheric height estimation by means of SAR is yet not established. In this article, a new estimator that allows the simultaneous estimation of TEC and ionospheric height from FR measurement is proposed. It exploits the variation of the parallel-to-LOS component of the geomagnetic field across azimuth sublooks. The performance of the proposed estimator is demonstrated using ALOS-2/PALSAR-2 data. The achieved estimation accuracy, precision, and the prerequisite for an accurate estimation are discussed.**

***Index Terms*—Earth ionosphere, Faraday rotation (FR), radar polarimetry, synthetic aperture radar (SAR), total electron content (TEC).**

I. Introduction

EARTH'S ionosphere distorts the amplitude, phase, and polarization of the transmitted and scattered Synthetic Aperture Radar (SAR) pulses (compared to the free space propagation) introducing a number of distortions in SAR images acquired by spaceborne configurations especially when operated at lower frequencies. The most prominent distortions are relative and absolute range/azimuth displacements [1], [2], radiometric biases [3]–[5], range and azimuth defocusing [6], and Faraday rotation (FR) [7], [8] attributed to the phase advance and/or time delay in the ionosphere. The strength of the individual distortions depends on the free electron concentration along the propagation path of the transmitted and scattered pulses through the ionosphere and its spatial and temporal variability at scales relevant for the SAR image formation process. The level of electron concentration in the ionosphere is expressed usually in terms of total electron content (TEC), which means the integrated number density of the electrons. One TEC unit (TECU) refers to 10^{16} electrons/m^2. The mean TEC levels in Earth's ionosphere are about few tens TECU, but during solar maximum often exceed 100 TECU.

At the presence of Earth's magnetic field, the ionosphere becomes birefringent and distorts the polarization state of the transmitted and scattered SAR pulses traveling through by rotating their polarization plane [9]. The rotation angle is known as FR angle and depends on the electron concentration in the ionosphere (i.e., the TEC level) and the projection of the (unit) wave propagation vector on the geomagnetic field. This dependency of the FR on the orientation of the radar line-of-sight (LOS) with respect to the geomagnetic field imposes an intrinsic dependency of the FR to TEC conversion performance on the imaging geometry employed. At high latitudes, for polar Low Earth Orbit (LEO) SAR orbits, the LOS and the geomagnetic field are widely parallel imposing a high sensitivity of FR to TEC, and allowing a precise TEC estimation from FR measurements. At low latitudes, however, the LOS and the geomagnetic field are getting more and more orthogonal to each other, limiting the sensitivity of the FR to TEC, and making the TEC estimation from FR measurements less precise. In this case, reliable TEC estimates require strong spatial averaging, which in turn prevents the estimation of small-scale ionospheric structures.

Typical quad-pol SAR configurations allow, at most latitudes (i.e., mid- and high-latitudes), the estimation of FR with centi-degree accuracy [10], [11], opening the door for a TEC estimation at km-level spatial resolutions with sub-TECU accuracy [1], [12]. But the FR to TEC conversion requires the knowledge of the imaging geometry (i.e., of the wave propagation vector) and the geomagnetic field along the propagation path. Because the geomagnetic field varies with height, uncertainties in the knowledge of the ionospheric height directly impact the TEC estimates. However, the fact that electron density distribution extends from 100 up to thousands of kilometers makes the definition of the ionospheric height challenging. In the context

Manuscript received July 14, 2020; revised October 10, 2020, December 24, 2020, March 15, 2021, and April 28, 2021; accepted May 13, 2021. Date of publication May 31, 2021; date of current version June 30, 2021. *(Corresponding author: Jun Su Kim.)*

The authors are with the German Aerospace Center (DLR), Wessling 82205, Germany (e-mail: junsu.kim@dlr.de; kostas.papathanassiou@dlr.de).

Digital Object Identifier 10.1109/JSTARS.2021.3085130

of this article, the ionospheric height refers to the height, where the geometry yields the true TEC after FR to TEC conversion (a detailed discussion follows in Section II). It corresponds to the center of mass of the electron density distribution weighted by the parallel-to-LOS component, i.e., the inner product $\vec{B} \cdot \hat{\kappa}$, of the geomagnetic field rather than to the peak of electron density distribution (usually located at around 300 to 400 km height).

Ionospheric electron density profiles are measured by ionosonde or incoherent ionospheric scatter radar [13], or derived from GPS occultation measurements [14]. However, the spatial and/or temporal sampling and resolution of such measurements are not sufficient for the correction/inversion of SAR data in an operational sense. Ionospheric models are able to predict ionospheric heights [15] but their application is constrained by the required initialization parameters that are, in general, not everywhere/anytime available. In this light, the estimation of the ionospheric height from the SAR data itself appears necessary. Indeed, several such attempts have been recently reported [16]–[18]. All of them rely on parallactic correlation measurements in azimuth, i.e., across azimuth subaperture images. However, by definition, such approaches depend on the presence of "noticeable" ionospheric variability within the synthetic aperture as well as sufficient contrast within the SAR image (i.e., scene).

In this article, a new approach that allows the simultaneous estimation of TEC and ionospheric height from FR measurement is proposed exploiting the variation of the parallel-to-LOS component of the geomagnetic field across azimuth sublooks. The azimuth beamwidth of conventional and contemporary spaceborne SAR systems is rather small (on the order of few degrees) so that often the same imaging geometry across the whole synthetic aperture can be assumed. However, the parallel-to-LOS component of the geomagnetic field changes noticeably across the synthetic aperture, especially as the geomagnetic field becomes more and more orthogonal to LOS (i.e., at lower latitudes—equatorial geometries). This variation of $\vec{B} \cdot \hat{\kappa}$ across the synthetic aperture and the associated squint dependency of FR is exploited for the simultaneous estimation of TEC and ionospheric height. In Section II, the formulation of FR in a squinted SAR geometry and its conversion to TEC for a given ionospheric height is addressed. This leads to a set of equations that allow the simultaneous estimation of TEC and ionospheric height. In Section III, the proposed methodology is applied on a sequence of quad-polarimetric ALOS-2 PALSAR-2 data acquired in 2015 across the Kalimantan Island in Indonesia that crosses the geomagnetic equator. The performance of the proposed methodology and the estimation accuracy of TEC and ionospheric height is discussed in terms of standard deviation and bias in Section IV. The effect of TEC gradient is formalized, and its compensation is addressed. Section V concludes this article.

II. Theory

A. FR to TEC

At the presence of the geomagnetic field, Earth's ionosphere becomes anisotropic for microwaves. Any polarized wave (e.g., polarized SAR pulse) traveling through the ionosphere can be decomposed into the two circular polarized waves rotating in opposite senses (left and right circular polarizations known as eigenpolarizations in the ionosphere), which propagate independently with different phase velocities. When recombined (after leaving the ionosphere), the polarization of the resulting wave (e.g., pulse) is changed with respect to the original one due to the phase difference between the two eigenpolarizations induced by the ionosphere. Strictly speaking, it is a rotation of the polarization plane of the wave by an angle that equals a quarter of the phase difference between two circular eigenpolarizations known as the FR angle. In the backscatter alignment convention, FR is cumulative: the reversal of propagation direction in backscattering does not cancel out the FR that occurred during the propagation in the transmission direction, but adds up [9], [19].

The increment of FR (Ω) is proportional to both the volume density of free electrons along the propagation path and the component of the geomagnetic field parallel to the LOS:

$$\Omega = \frac{e}{c m_e f^2} \int_C n_e\left(C\left(l\right); l\right)\ \hat{\kappa} \cdot \vec{B}\, dl \tag{1}$$

where $\vec{B}$ is the geomagnetic field, $\hat{\kappa}$ is the unit propagation vector, c is the speed of light, f is the center carrier frequency, and m_e and e are the electron mass and charge, respectively. $C = C(l)$ is the propagation path parameterized in terms of l, with $dC/dl = \hat{\kappa}$ and $n_e(C(l); l)$ is the volume density of free electrons along the propagation path.

In the SAR imaging geometry, each point along $C(l)$ is uniquely mapped into a height h above the Earth ellipsoid, so that the electron density profile $n_e(l)$ can be reparameterized with respect to h. The TEC is given by the integration of electron density $n_e(l)$ along $C(l)$:

$$\mathrm{TEC} = \int_C n_e\left(C\left(l\right); l\right) dl\ . \tag{2}$$

The TEC in (2) is known as slant TEC (sTEC) as it is integrated along the slanted SAR propagation direction. It is linked to the vertical TEC (i.e., the TEC obtained when integrating in nadir direction) by the local incidence angle θ at the ionospheric piercing point $\mathrm{sTEC}\ \cos\theta = \mathrm{TEC}$. The local incidence angle θ varies along the propagation path due to Earth's spherical shape. In the following, for the sake of convenience, TEC refers to sTEC.

Equations (1) and (2) indicate that for an accurate conversion of FR estimates to TEC the knowledge of $n_e(l)$ and $\vec{B}$ along the LOS is required as $\vec{B}$ varies along the integration path.

To bypass the lack of knowledge of the $n_e(l)$ profile, the so-called thin-layer approximation is employed: the distribution of $n_e(l)$ is reduced to $n_e\ (h) = \ \delta(h - h_{\mathrm{iono}}) \cdot \mathrm{TEC}$, where δ is the Dirac delta function and h_{iono} is the so-called ionospheric height. The intermediate value theorem guarantees the existence of such an h_{iono} that yields the true TEC in the interval of $(0,\ h_{\mathrm{sat}})$, where h_{sat} denotes the SAR orbit altitude [16]. The value of h_{iono} corresponds to the center of mass of the $n_e \cdot (\vec{B} \cdot \hat{\kappa})$ profile in the given interval. Now, the FR in (1)

reduces to

$$\Omega = \zeta \frac{e\vec{B}\cdot\hat{\kappa}}{cm_e f^2}\mathrm{TEC} \tag{3}$$

with $\zeta = \frac{c^2 r_e}{2\pi} \approx 40.31$ m^3/s^2, where r_e is the classical electron radius. In (3), $\vec{B} = \vec{B}\,(h_{\mathrm{iono}})$ is understood as the geomagnetic field at h_{iono}. Under this condition, TEC and the FR become proportional to each other. However, as the geomagnetic field changes with height, the conversion of FR to TEC by means of (3) still requires the knowledge of the ionospheric height to determine $\vec{B}\cdot\hat{\kappa}$. As a reference of required accuracy, averaged over the globe, an ionospheric height uncertainty of 100 km leads to a 5% TEC uncertainty. The TEC uncertainty is larger at equatorial latitudes and smaller at polar ones.

Conventional FR-to-TEC conversion relies on (3) where estimated FR values are converted to TEC levels assuming a given (fixed) h_{iono} [11], [12], [16].

B. Squint Dependency

Most spaceborne SAR configurations on a sun-synchronous LEO operate on a polar orbit with an inclination of about 98°. For JAXA's ALOS-2, the orbit inclination is 97.92°. At lower heights, near to Earth's surface, the geomagnetic field can be approximated by a dipole field with poles coinciding with the geographic poles in a most simple approximation. The radial and latitudinal components of such a dipole magnetic field at an orbital radius R_{orbit} and latitude ϕ are given by

$$\begin{aligned} B_r &= -\frac{2B_0}{R^3}\sin\phi \\ B_\theta &= \frac{B_0}{R^3}\cos\phi \end{aligned} \tag{4}$$

where $R = R_{\mathrm{orbit}}/R_E$ expresses the orbit radius R_{orbit} relative to the Earth's mean radius R_E, and $B_0 = 3.07\times10^{-5}$ T [20]. For a given orbital position, the nadir direction is simply the opposite of the radial direction, i.e., $\vec{B}\cdot\hat{\kappa} = -B_r$. In a squinted SAR geometry, the squint angle β modifies $\vec{B}\cdot\hat{\kappa}$ as

$$\vec{B}\cdot\hat{\kappa} = -B_r\cos\beta + B_\theta\sin\beta \tag{5}$$

and the dependency of $\vec{B}\cdot\hat{\kappa}$ on β is given by

$$\frac{d}{d\beta}\vec{B}\cdot\hat{\kappa} = B_r\sin\beta + B_\theta\cos\beta \approx B_\theta. \tag{6}$$

It is noteworthy that the sensitivity of $\vec{B}\cdot\hat{\kappa}$ on the squint angle β reaches its maximum at the geomagnetic equator (i.e., at low latitudes), where $\vec{B}\cdot\hat{\kappa}$ itself becomes zero making the conversion of FR to the TEC unfavorable if not impossible.

In reality, the orbits are inclined and the sensors illuminate obliquely. For a satellite moving with forward velocity $\vec{v}_{\mathrm{sat}}$ in direction $\hat{v}_0 = \vec{v}_{\mathrm{sat}}/|\vec{v}_{\mathrm{sat}}|$, the change of squint angle is associated to an LOS change as $\hat{\kappa}(\beta) = \cos\beta\,\hat{\kappa}_0 + \sin\beta\hat{v}_0$, where $\hat{\kappa}_0$ is the unit propagation vector at the zero-Doppler geometry. The derivative of $\vec{B}\cdot\hat{\kappa}$ with respect to the squint angle β around zero-Doppler becomes $d(\vec{B}\cdot\hat{\kappa})/d\beta = \vec{B}\cdot\hat{v}_0$, leaving active only the parallel component of the geomagnetic field in the direction the satellite moves.

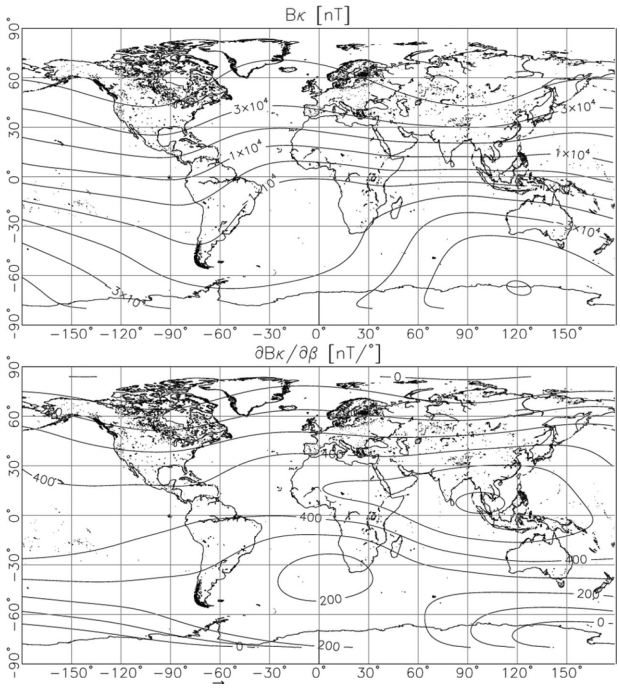

Fig. 1. Estimates of $\vec{B}\cdot\hat{\kappa}$ (top) and its sensitivity on squint angle β. Ascending orbit at 630 km and ionospheric height of 300 km is assumed for the calculation. Unit is nT at top and nT/° at bottom.

Fig. 1 shows a map of $\vec{B}\cdot\hat{\kappa}_0$ (top) and $d(\vec{B}\cdot\hat{\kappa})/d\beta$ (bottom) for a sun-synchronous orbit at 630 km altitude (e.g., ALOS-2) for an off-nadir angle of 30° and an ionospheric height of 300 km. For an ascending orbit, the sign of $d(\vec{B}\cdot\hat{\kappa})/d\beta$ is widely positive, as the geomagnetic field is oriented toward the north. As expected from (6), the sensitivity of $\vec{B}\cdot\hat{\kappa}$ to the squint has its maximum in the equatorial zone and decreases with increasing latitude. For a large portion of the equatorial zone, the squint sensitivity is more than 500 nT/°.

The derivative of (3) with respect to β can be written as

$$\begin{aligned} \frac{d\Omega}{d\beta} &= \frac{\zeta e}{cm_e f^2}\,\mathrm{TEC}\,\frac{d\left(\vec{B}\cdot\hat{\kappa}\right)}{d\beta} = \zeta\frac{e\vec{B}\cdot\hat{v}_0}{cm_e f^2}\mathrm{TEC}.\,\frac{d\Omega}{d\left(\vec{B}\cdot\hat{\kappa}\right)} \\ &= \frac{\zeta e}{cm_e f^2}\,\mathrm{TEC}. \end{aligned} \tag{7}$$

Note that $\hat{\kappa}$ is a function of the squint angle β and $\vec{B}$ is a function of ionospheric height h_{iono}; therefore, $\vec{B}\cdot\hat{\kappa}$ depends on both: the squint angle β and the ionospheric height h_{iono}. Hereafter, the constant $K = (\zeta e)/(cmf^2)$ is introduced for the sake of brevity. For ALOS-2/PALSAR-2, $K = 1.5467\times10^{-14}$ m^2/T ($f = 1.2365$ GHz).

Equations (3) and (7) provide two equations with two unknowns, namely the ionospheric height h_{iono} and TEC, allowing the estimation of h_{iono} and TEC. It is important to note that (3) and (7) are both proportional to TEC. The implications this relation has on the ionospheric height and TEC inversion will be discussed in detail in Section III-B.

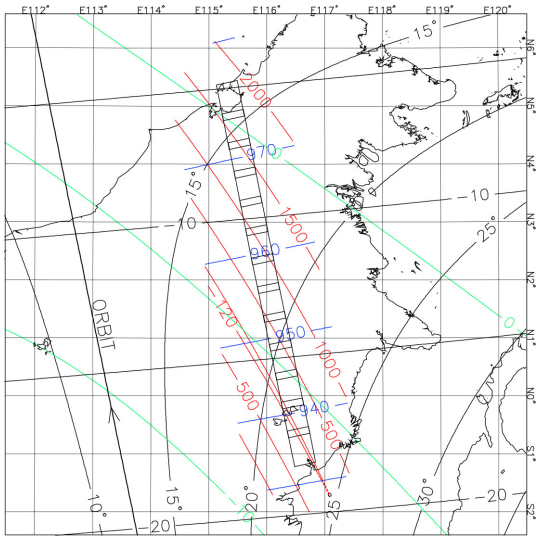

Fig. 2. Footprints of ALOS-2 PALSAR-2 sequential Kalimantan Island (sequence of rectangles). The nadir track of orbit and its direction is shown together. The black horizontal contours indicate the magnetic dip angles in degree. The green oblique contours indicate the $\vec{B} \cdot \hat{\kappa}$ calculated at 300 km altitude in the unit of 1000 nT. The black curvy contours indicate the geomagnetic field angles, i.e., the angle of the projected geomagnetic field with respect to the azimuth direction. The red contours around the footprints indicate the height-spread of $\vec{B} \cdot \hat{\kappa}$, and the blue contours are the azimuth-spread of $\vec{B} \cdot \hat{\kappa}$, both in nT unit.

III. Experimental Data Analysis

A. Data

The dataset used consists of a 13 consecutive fully polarimetric datasets acquired by ALOS-2 PALSAR-2 in beam FP6-4 high sensitive mode on April 27th, 2015 along the ascending orbit (i.e., from south to north), imaging a 740 km long strip along Kalimantan island in Indonesia, (scene ID's: ALOS2 05005 7170—ALOS2 05006 0090). The footprints and the nadir track of the orbit are plotted in Fig. 2. The horizontal contours indicate the geomagnetic dip angle in degrees, i.e., the angle the geomagnetic field forms with the horizontal plane. The geomagnetic field is estimated using the coefficients of the spherical harmonics provided from International Geomagnetic Reference Field (IGRF) [21] at an altitude of 300 km. Although most of the acquisitions are in the (geographic) northern hemisphere, the geomagnetic dip angles are negative (ranging from –5° to –20°) throughout the whole sequence. The $\vec{B} \cdot \hat{\kappa}$ values at 300 km height are indicated by the green contour lines in units of 1000 nT, starting at –7000 nT at the beginning of the sequence (the southern part), and reach 0 nT at the end (the northern tip) of the sequence. The difference of maximum and minimum $\vec{B} \cdot \hat{\kappa}$ along the LOS is indicated by the red contours and will be referred in the following as the height-spread of $\vec{B} \cdot \hat{\kappa}$. Accordingly, the height-spread of $\vec{B} \cdot \hat{\kappa}$ is smallest at the beginning of the sequence and increases with increasing latitude (northwards). Especially close to the geomagnetic equator, where the vertical component of the geomagnetic field is small, the horizontal east–west component becomes the main geomagnetic field contribution parallel to LOS. Note that the extrema of $\vec{B} \cdot \hat{\kappa}$ along the LOS may not necessarily be at the endpoints of the LOS interval.

The blue contours around the footprints indicate the change of $\vec{B} \cdot \hat{\kappa}$ across the synthetic aperture. This range of $\vec{B} \cdot \hat{\kappa}$ values will be referred in the following as azimuth-spread and is obtained by multiplying the beamwidth (in this observation mode 1.6°) with $d(\vec{B} \cdot \hat{\kappa})/d\beta$. In Fig 2, azimuth-spread increases with increasing latitude but the increment is so small that it can be practically neglected.

The hyperbolic black contours in Fig. 2 indicate the geomagnetic field angle in degrees [22], i.e., the angle formed by the azimuth direction (given by $\hat{v}_0$) and the geomagnetic field vector projected onto a horizontal plane on the ionospheric heights along the LOS. The southern scenes of the sequence are affected by equatorial plasma bubbles inducing a stripe pattern in the SAR image. Note that the spectral correlation of the stripe pattern in azimuth, i.e., the amplitude correlation across azimuth sublooks, can be used to estimate their height and drifting velocity in favorable geometries (i.e., at small geomagnetic field angles where the stripes become parallel aligned to the azimuth direction) [22].

Fig. 3 shows the Pauli RGB representation of the scene (first row), the FR estimates (second row), the change of the $\vec{B} \cdot \hat{\kappa}$ component at different heights (third row), and the stripe pattern (fourth row). The two axes superimposed on the Pauli image indicate the zero-Doppler time in UTC and ground distance along the azimuth in km. The Pauli RGB image (first row) indicates that the southern part of the sequence is swampy characterized by low backscatter levels, while the northern part consists by dense forested areas and significant topographic variability. The FR map estimated from the data is shown in the second row of Fig. 3. The map indicates an increasing FR from left to right. At the southern part of the sequence, FR starts at a level of –2.5° and gradually increases to 0° when moving toward the northern part. The $\vec{B} \cdot \hat{\kappa}$ variation across the sequence at different ionospheric heights as estimated by using the IGRF model [21] at the scene center for a zero-Doppler geometry is plotted on the third row of Fig. 3: From $h_{\text{iono}} = 100$ to 600 km, the colors change from violet to red in 100 km steps. The height-spread of $\vec{B} \cdot \hat{\kappa}$ is at the beginning of the sequence (the southern part) very small and increases significantly when moving toward the end of the sequence (northern part) reaching more than 1500 nT (see Fig. 2 and third row Fig. 3). An important implication of the height-spread of $\vec{B} \cdot \hat{\kappa}$ is that the (geographic) location where $\vec{B} \cdot \hat{\kappa} = 0$ depends on the ionospheric height. A variation of the ionospheric height about 100 km is associated by a shift of about 30 km in the location where $\vec{B} \cdot \hat{\kappa} = 0$ holds.

At the bottom of Fig. 3, the amplitude image of the "stripe"-pattern is shown, which is obtained by normalizing the azimuth sub-band power to the full-band power. The deformation induced by the topography has been compensated [22]. This pattern of parallel linear amplitude undulations aligned to the geomagnetic field angle [4], [5] is the result of SAR imaging through plasma bubbles elongated along the geomagnetic field at the post-sunset sector of the equatorial ionosphere. The stripe patterns do not appear at the northern part of the sequence.

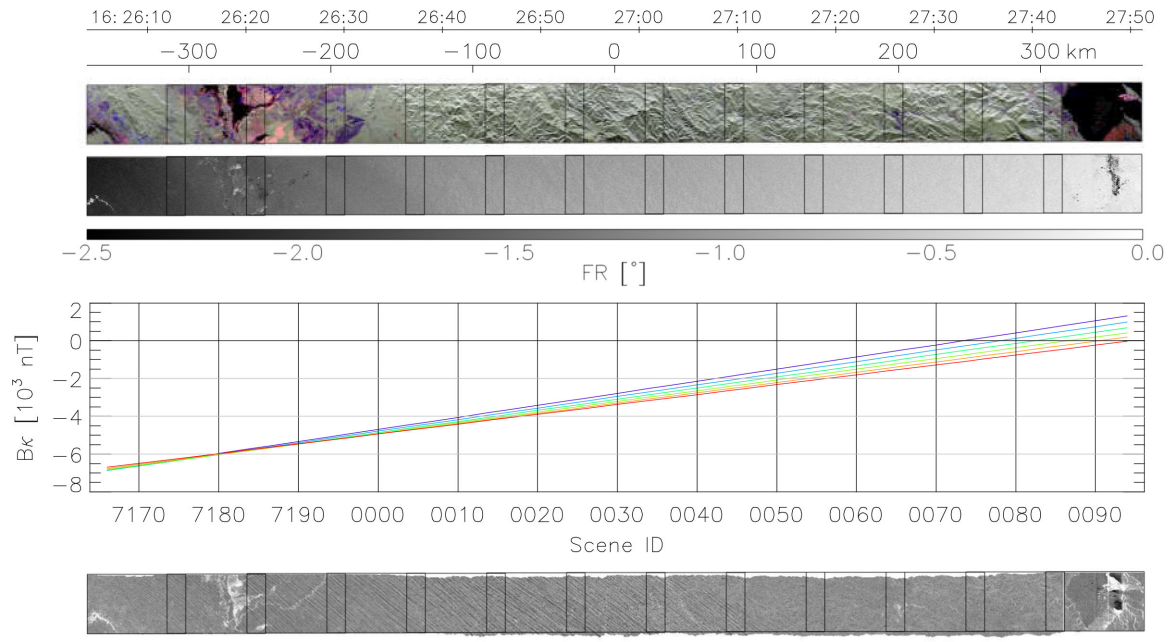

Fig. 3. (Top) Pauli-decomposition image, (second row) Faraday rotation, (third row) the change of $\vec{B} \cdot \hat{\kappa}$ across the sequence estimated at each scene center at different altitudes (violet to red from 100 to 600 km with 100 km step), and (bottom) the amplitude "stripe"-pattern. Note the shift of $\vec{B} \cdot \hat{\kappa} = 0$ position with respect to ionospheric height and corresponding FR values indicating their bias.

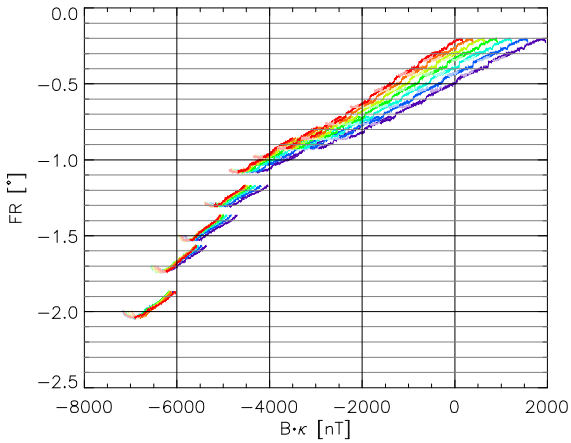

Fig. 4. "Bk–FR plot" of ALOS-2 PALSAR-2 data across Kalimantan Island. The FR estimates from the 13 scenes are plotted from bottom left to top right. Per each scene, the dependency of FR on parallel to LOS component of geomagnetic field ($\vec{B} \cdot \hat{\kappa}$) is plotted. $\vec{B} \cdot \hat{\kappa}$ is the proxy of the squint. The different colors indicate the altitude where $\vec{B} \cdot \hat{\kappa}$ is calculated (at the ground, 100, 200, 300, 400, 500, and 600 km altitudes from violet to red). The high saturation of the colors highlights where the FR and $\vec{B} \cdot \hat{\kappa}$ obeys linear relations in (7).

B. Bk–FR Plot

The change of FR as a function of the squint angle β is obtained by estimating the FR in the Doppler frequency domain. The obtained FR estimates for all 13 scenes are plotted on the "Bk–FR plot" in Fig. 4. Each of the 13 vertically separated groups of FR estimates corresponds to a scene. Because for each squint angle $\vec{B} \cdot \hat{\kappa}$ depends on the height, multiple $\vec{B} \cdot \hat{\kappa}$—$\Omega$ relations are possible. The different colors within a group indicate the different ionospheric heights, at which $\vec{B} \cdot \hat{\kappa}$ is calculated: from violet to red, the ionospheric altitude changes from 100 to 600 km in steps of 100 km. The southern scenes, represented in the bottom-left section of the "Bk–FR plot," are characterized by small(er) FR levels and their height-spread is small. The northern scenes in the top-right section of the plot show high(er) FR levels and a large(r) height-spread.

According to (3) and (7), each line in Fig. 4 at a fixed height should be straight as the change of FR across the azimuth sub-bands is expected to be a linear function of the squint angle. However, at (very) high azimuth frequencies (at the left tips of the colored line), the obtained Bk–FR relation is no longer linear as indicated by the lower color saturation in Fig. 4. One reason for this may be residual polarimetric system distortion across the Doppler frequency (for example, induced by the antenna patterns), which are not compensated during the conventional polarimetric calibration [23]. Such a frequency-dependent residual polarimetric system distortion is not an exclusive azimuth effect but is known to appear in range as well [24]. In the following, only Doppler frequencies where the linearity of the FR change is preserved are considered to estimate $\partial\Omega/\partial(\vec{B} \cdot \hat{\kappa})$.

Comparison of FR and $\vec{B} \cdot \hat{\kappa}$ in Fig. 4 indicates that the estimated FR values are biased by about –0.35° (assuming an ionospheric height of 300 km) as the FR remains nonzero for $\vec{B} \cdot \hat{\kappa} = 0$ regardless of the selection of the ionospheric height. As a result, the FR estimates remain negative along the whole sequence even when crossing the $\vec{B} \cdot \hat{\kappa} = 0$ condition. Attributing this bias to the inaccuracy of the geomagnetic field model is rather unrealistic, as it corresponds to a deviation of about 2000 nT (associated with the shift of the x-axis in Fig. 4 required to move the origin to the extension of the Bk–FR line). This is excessive to be attributed to the uncertainty of

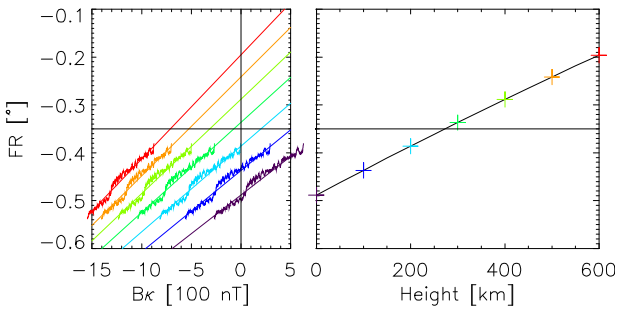

Fig. 5. Best fitting lines at different heights at ground to 600 km with 100 km step colored from violet to red (left), and the y-intersection curve (right).

the geomagnetic model. The effect of the magnetizing sources in the crust, which are not accounted by the global geomagnetic models, is negligible at the ionospheric height. Sources in the ionosphere may change the geomagnetic field but only on the order of about 10 nT (on calm conditions [26] as the case for the actual observation time characterized by Kp 1+ [27]).

More likely is that the FR bias is largely caused by a residual system distortion (cross-talk) component resulting from an imperfect separation of FR from system distortion during calibration [23]–[25]. Indeed, a residual cross-talk contribution of about -44dB is sufficient to introduce an FR bias of about –0.35°. In the following, the bias has been compensated by shifting the y-axis in Fig. 4 by as much as –0.35°.

In addition, a second correction of the dataset is necessary to compensate for the discontinuity of the FR estimates obtained in the transition from negatives to positives Doppler frequencies. This discontinuity is compensated by adding an offset of 0.001 radian to the FR estimates at positive Doppler frequencies. This offset is probably related to the Dual Receive Channel architecture of the PALSAR-2 antenna and may vary from acquisition to acquisitions depending on the operation mode employed but also the settings of the processor. Not accounting for this offset introduces a distortion of the linear Bk–FR relation estimation.

Equations (3) and (7) require the straight-line segments on the "Bk–FR plot" to pass through the origin. This condition is fulfilled only at a single ionospheric height. The best fitting line of a given Bk–FR line for a height is written as

$$\Omega \;=\; m\left(\vec{B}\cdot\hat{\kappa}\right)+\Omega_0 \tag{8}$$

where m and Ω_0 are the slope and the y-intersection on the Bk–FR plane. Both are functions of the ionospheric height h. Let us call the function $\Omega_0(h)$ the y-intersection curve. It draws an oblique almost straight gentle curve. Ideally, the ionospheric height is found as $h_{\rm iono}=\Omega_0^{-1}\,(0)$. However, here, due to the FR bias discussed above, $h_{\rm iono}=\Omega_0^{-1}\,(-0.35^\circ)$. The TEC is direct proportional to the slope m of the origin-passing h:

$$\mathrm{TEC} \;=\frac{m}{K}\,. \tag{9}$$

Equation (9) is a simple paraphrase of (7).

Fig. 5 shows an example of ionospheric height estimation by means of (8). On the left, the best fitting lines at different altitudes are shown from 0 (violet) to 600 km (red) in 100 km steps. The ridged lines are the FR estimates, and the straight lines the line-fitted relations. It is obvious that the y-intersection Ω_0 increases gradually with increasing height as a result of the gradual decrease of the geomagnetic field with height. On the right, Ω_0 is plotted against ionospheric height. There is one intersection point where Ω_0 becomes –0.35°, the level of the supposed FR bias. Accordingly, the associated height, slightly lower than 300 km, is the wanted ionospheric height.

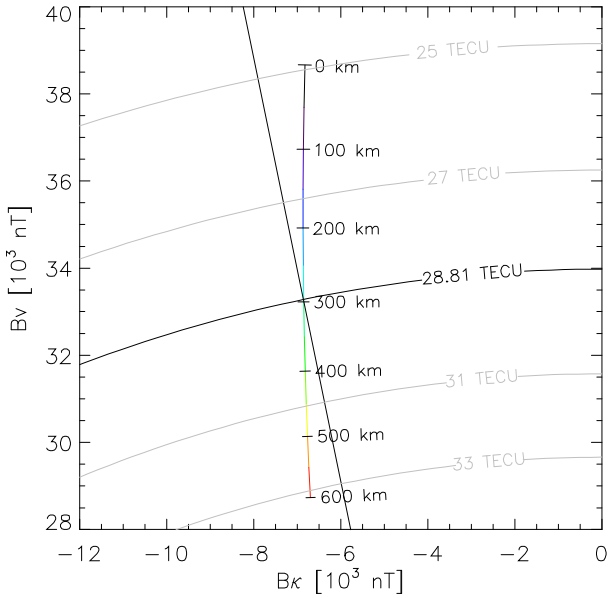

Fig. 6. Alternative representation of TEC and ionospheric height estimation based on the orthogonality of zero-Doppler vector and azimuth direction.

The estimation of the ionospheric height and TEC can also be interpreted in an alternative way, exploring the orthogonality of $\hat{\kappa}_0$ and $\hat{v}_0$. Accordingly, it is possible to define a plane spanned by $\vec{B}\cdot\hat{\kappa}_0$ and $\vec{B}\cdot\hat{v}_0$. For the given observation location and geometry, the trajectory of $\vec{B}\cdot\hat{\kappa}_0$ and $\vec{B}\cdot\hat{v}_0$ as a function of height is estimated and plotted as a colored curve in Fig. 6.

Combining (3) and (7)

$$\left(\vec{B}\cdot\hat{\kappa}_0,\vec{B}\cdot\hat{v}_0\right)=\frac{1}{K\cdot\mathrm{TEC}}\left(\Omega,\frac{\partial\Omega}{\partial\beta}\right) \tag{10}$$

is obtained indicating that the FR estimates are projected on a ray through $(\vec{B}\cdot\hat{\kappa}_0,\ \vec{B}\cdot\hat{v}_0)=(0,\ 0)$. The intersection between the trajectory and the ray provides the information for both height and TEC. The height is derived from the parameterization of the trajectory, and the TEC is inversely proportional to the radius of the intersection.

In Fig. 6, the colored trajectory $(\vec{B}\cdot\hat{\kappa}_0,\vec{B}\cdot\hat{v}_0)$ shows the overall decrease of the geomagnetic field with increasing height. The radial straight line is in the direction of $(\Omega,\frac{\partial\Omega}{\partial\beta})$. They intersect each other at around 300 km height. The radius of the intersection corresponds to the TEC level to be 28.81 TECU.

This alternative representation in Fig. 6 demonstrates intuitively the estimation of the two parameters. However, the radius and TEC are related through the observation of $(\Omega,\frac{\partial\Omega}{\partial\beta})$, which varies from dataset to dataset. Overlapping the estimates from multiple datasets on Fig. 6 does not help grasping the regional

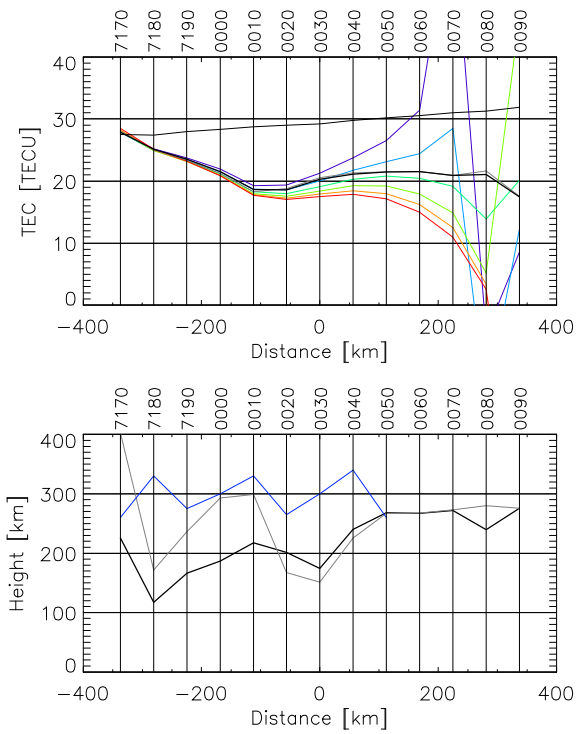

Fig. 7. (Top) estimated TEC values using proposed method (black) and those at fixed altitudes: (violet to red from 100 to 600 km with 100 km step). The straight line around 30 TECU is the TEC derived from the interpolation of IGN data. (Bottom) the estimated ionospheric height using the proposed method (grey), TEC gradient compensated estimate (tick black See Section IV-C.) and using the stripe angles (blue).

trend of TEC and ionospheric height. This is why the "Bk–FR plot" (Fig. 4) is preferred.

C. Results

The achieved estimates of TEC and ionospheric height are shown in Fig. 7. The TEC estimates are shown on the top (grey line): there is a decrease of TEC about 10 TECU in the first 200 km that levels off later at around 20 TECU. The colored lines indicate the TEC estimates obtained by fixing the ionospheric heights from 100 to 600 km with 100 km steps with different colors from violet to red. The dashed black line indicates the TEC levels interpolated from the international GNSS network [28] that seems to confirm a slowly increasing TEC trend of about 30 TECU.

The fixed altitude TEC estimates diverge as $\vec{B} \cdot \hat{\kappa}$ approaches zero. In such conditions, the sensitivity of TEC to $\vec{B} \cdot \hat{\kappa}$ becomes so high [see (3)], that the height-spread of $\vec{B} \cdot \hat{\kappa}$ leads to an (unreasonable) large bias in the converted TEC estimates. Approaching to $\vec{B} \cdot \hat{\kappa} = 0$, the estimated TEC degrades fast indicating that the assumed ionospheric heights do not match. In contrast, the TEC estimates obtained from the proposed approach (grey) remain surprisingly stable even when the fixed ionospheric height approach fails to provide stable solutions.

The obtained TEC estimates clearly indicate the advantage of the proposed approach especially when $\vec{B} \cdot \hat{\kappa}$ is small. At the same time, the associated ionospheric height estimates, given by the grey line in the bottom plot of Fig. 7, indicates its limitation. The obtained ionospheric height estimates are stable at the northern part of the sequence (about at 270 km), but become unstable fluctuating within a two-hundreds kilometers of height range at the southern part of the sequence. At a first glance, the main reason for this instability appears to be due to the reduced height-spread of $\vec{B} \cdot \hat{\kappa}$, but this will be proven not to be the case in Section IV-C. Anyway, even in the cases where the height estimate becomes unstable, the TEC conversion remains stable because TEC is insensitive to the ionospheric height when the height-spread of $\vec{B} \cdot \hat{\kappa}$ is small. This is why the TEC estimates at the southern part of the sequence remain stable regardless of the selection of height (given by the colored lines that are all at the same positions), while the ionospheric height estimates fluctuate.

The blue line in bottom of Fig. 7 represents the ionospheric height estimates obtained from the spectral correlation analysis in the southern part of the sequence. The large geomagnetic field angle makes in this case an accurate ionospheric height and drift velocity by means of spectral correlation not possible [22] even if ionospheric disturbances are present. In this case, reliable height estimates are still possible when the drift is known or fixed. However, in the absence of stripe-pattern like distortions no estimation is possible. For the given geometry, an error of 100 m/s in the eastward drift velocity leads to an underestimation of the ionospheric height of about 20 km. The ionospheric height estimates obtained from the spectral correlation of the stripe pattern do not agree with the estimates obtained using the proposed approach probably because of the height estimation instability in the southern part of the sequence. However, another plausible reason for this is that the plasma bubbles, i.e., the source of the stripe patterns, may indeed be located at a different height than the center of mass of the electron density distribution.

IV. Estimation Performance

A. TEC Estimation

In this section, the TEC estimation performance of the proposed approach is evaluated and compared against the conventional FR-to-TEC conversion approach [i.e., (3)] [8], [12], [16]. The fact that multiple independent sublook FR estimates are used to estimate the line segment in the "Bk–FR plot" makes the proposed TEC estimation in general inferior compared to the conventional FR-to-TEC conversion performance that relies on single FR estimates obtained by using a larger number of looks. According to the proposed approach, for the TEC estimation, a SAR image segment of $N \times M$ (range $\times$ azimuth) samples is Fourier transformed in azimuth direction to reveal the (linear) squint dependency of the FR. The variance of the slope estimate (m) of the linear fit ($y = mx + n$) is

$$\sigma_m^2 = \frac{1}{p-2} \frac{\sum_i (y_i - \hat{y}_i)^2}{\sum_i (x_i - \bar{x})^2} \tag{11}$$

where p is the number of samples, $\hat{y}_i = mx_i + n$, and $\bar{x} = \sum_i x_i / p$ is the mean of x. $p = M$ for the M samples in azimuth direction. The numerator $\sum_i' (y_i - \hat{y}_i)^2$ expresses the sum of

variances of all FR estimates

$$\sum_i (y_i - \hat{y}_i)^2 = \frac{M\left(1-\gamma_{\rm pol}^2\right)}{32\gamma_{\rm pol}^2 N}. \tag{12}$$

The denominator of (11) is related to the $\vec{B}\cdot\hat{\kappa}$ sampling. The spatial sampling in azimuth direction is (after the Fourier transform) PRF/M. Using the relation between Doppler frequency $f_{\rm az}$ and squint angle $\beta = (v_{\rm sat}/\rho_0 K_a) f_{\rm az}$ for a Doppler rate K_a, the value of $\vec{B}\cdot\hat{\kappa}$ for the kth azimuth index (zero-centered) is given by

$$\left(\vec{B}\cdot\hat{\kappa}\right)_k = \vec{B}\cdot\hat{\kappa}_0 + \left(\vec{B}\cdot\hat{v}_0\right)\frac{v_{\rm sat}}{\rho_0 K_a}\frac{\mathrm{PRF}}{M}k \tag{13}$$

where ρ_0 is the zero-Doppler range. Assuming a regular sampling, the denominator becomes

$$\sum_i (x_i - \bar{x})^2 = \frac{M^3}{12}\left(\left(\vec{B}\cdot\hat{v}_0\right)\frac{v_{\rm sat}}{\rho_0 K_a}\frac{\mathrm{PRF}}{M}\right)^2. \tag{14}$$

The variance of the TEC estimation is obtained by inserting (12) and (14) to (11) as

$$\sigma_{\rm TEC}^2 = \frac{3}{8}\frac{1}{\left(\left(\vec{B}\cdot\hat{v}_0\right)\frac{v_{\rm sat}\mathrm{PRF}}{\rho_0 K_a}\right)^2}\frac{1}{K^2}\frac{1-\gamma_{\rm pol}^2}{\gamma_{\rm pol}^2 NM}. \tag{15}$$

For reference, the TEC estimation accuracy from the conventional FR-to-TEC approach is given by (modified from [16])

$$\sigma_{\rm TEC}^2 = \frac{1}{32}\frac{1}{\left(\vec{B}\cdot\hat{\kappa}\right)^2}\frac{1}{K^2}\frac{1-\gamma_{\rm pol}^2}{\gamma_{\rm pol}^2 NM}. \tag{16}$$

Fig. 8 compares the two performances for a (very) large estimation window of $M = N = 10^4$ (roughly 50 km $\times$ 30 km for the ALOS-2 case) corresponding to 10^8 looks and a polarimetric coherence level of $\gamma_{\rm pol} = 0.95$. The standard deviation of the TEC estimation using the proposed approach [i.e., given by (14)] is shown on the top. As expected, the estimation performance is best close to the geomagnetic equator and reduces with increasing latitude. In the middle of Fig. 7, the standard deviation of the conventional FR-to-TEC conversion approach [i.e., given by (15)] is shown. Because of the large number of looks, the standard deviation of the TEC estimation is very small. The performance of the conventional approach is an order of two to three better than the performance of the proposed approach and fails only at a narrow belt of some hundreds of kilometers width centered on the geomagnetic equator where $\vec{B}\cdot\hat{\kappa}$ is (close to) zero (known as the equatorial gap). It is exactly there where the performance of the proposed approach becomes superior.

The unknown ionospheric height can bias the estimation of $\vec{B}\cdot\hat{\kappa}$, and thus that of TEC. The map at the bottom of Fig. 8 shows the deviation of the estimated TEC for a 100 km of ionospheric height change around 300 km under average TEC level. The high TEC inaccuracy along the equatorial gap of (close to) zero $\vec{B}\cdot\hat{\kappa}$ is clearly visible. An interesting feature is the presence of a belt with small TEC variation meandering north and south of the $\vec{B}\cdot\hat{\kappa} = 0$ region. It is where the height-spread of $\vec{B}\cdot\hat{\kappa}$ goes to zero.

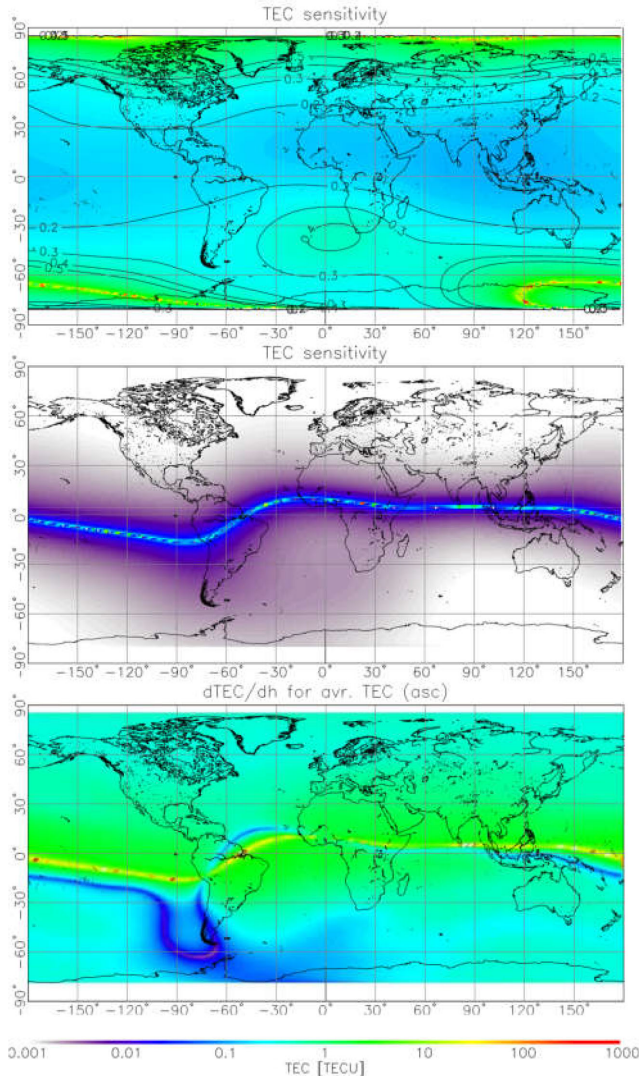

Fig. 8. Comparison of TEC estimation accuracies. (Top) the estimation accuracy of proposed method, (middle) that of conventional method, and (bottom) TEC variation for a 100-km ionospheric height error for average TEC level.

The main contribution to the total TEC estimation uncertainty (i.e., the sum of standard deviation and bias) is the ionospheric height uncertainty. A direct comparison of the maps on top and bottom of Fig. 8 is still not possible because the distribution of ionospheric height is not specified. However, it is clear that at least along the $\vec{B}\cdot\hat{\kappa} = 0$, the proposed approach estimates TEC better than the conventional one.

B. Height Estimation

The estimation accuracy of the ionospheric height is directly connected to the determination accuracy of Ω_0, and depends critically on the estimation accuracy of the slope of the Bk–FR line [see (8)]. The height estimation accuracy is given by multiplying the slope of the y-intersection curve, with the slope determination accuracy on the "Bk–FR plot." The latter has

already been discussed above [see (15)], so that now only the slope of the y-intersection curve remains to be discussed.

For the determination of the slope of the y-intersection curve, the starting point is a series of FR estimates associated to different Doppler frequencies, as shown on the left plot of Fig. 5. Each Doppler frequency is assigned to a different $\vec{B}\cdot\hat{\kappa}$ value [see (13)]. The assignment is also a function of the height h, at which the geomagnetic field is calculated, so that a change of h causes a change of the geomagnetic field and a displacement of the y-intersection point Ω_0. In this sense, applying the chain rule on the y-intersection curve leads to

$$\frac{d\Omega_0}{dh} = \frac{d\Omega_0}{d\left(\vec{B}\cdot\hat{\kappa}_0\right)}\frac{d\left(\vec{B}\cdot\hat{\kappa}_0\right)}{dh} + \frac{d\Omega_0}{d\left(\vec{B}\cdot\hat{v}_0\right)}\frac{d\left(\vec{B}\cdot\hat{v}_0\right)}{dh}. \tag{17}$$

The first term $d\Omega_0/d(\vec{B}\cdot\hat{\kappa}_0)$ indicates the change of the y-intersection as the x-coordinate on the "Bk–FR plot" shifts, and it is proportional to the slope m

$$\frac{d\Omega_0}{d\left(\vec{B}\cdot\hat{\kappa}\right)} = -m\,. \tag{18}$$

The second term is more complex because $\vec{B}\cdot\hat{v}_0$ does not appear explicitly. In the interpretation of "Bk–FR plot," the change of $\vec{B}\cdot\hat{v}_0$ is associated with the change of the azimuth-spread. The increase of azimuth-spread leads to a gentler slope, or reduces the slope m in positive slope cases: $dm/d\,(\vec{B}\cdot\hat{v}_0) = -m/(\vec{B}\cdot\hat{v}_0)$. Here, a consideration of negative slope values is not required because the TEC level is always positive. The slope m and y-intersection Ω_0 are related as $d\Omega_0/dm = -\vec{B}\cdot\hat{\kappa}$. Therefore,

$$\frac{d\Omega_0}{d\left(\vec{B}\cdot\hat{v}_0\right)} = m\frac{\vec{B}\cdot\hat{\kappa}_0}{\vec{B}\cdot\hat{v}_0}. \tag{19}$$

Finally, the slope of y-intersection curve becomes

$$\frac{d\Omega_0}{dh} = -m\left(\frac{d\left(\vec{B}\cdot\hat{\kappa}_0\right)}{dh} - \frac{\vec{B}\cdot\hat{\kappa}_0}{\vec{B}\cdot\hat{v}_0}\frac{d\left(\vec{B}\cdot\hat{v}_0\right)}{dh}\right). \tag{20}$$

Now, the height estimation accuracy is

$$\sigma_h = \frac{dh}{d\Omega_0}\cdot\sigma_{\Omega_0} = \frac{dh}{d\Omega_0}\left(\vec{B}\cdot\hat{\kappa}_0\right)\sigma_m. \tag{21}$$

A very important conclusion of this analysis is that the ionospheric height estimation accuracy is inversely proportional to m, which is proportional to TEC. In other words, with increasing TEC level the height estimation becomes more accurate.

Fig. 9 shows the ionospheric height estimation accuracy for the mean level of TEC during the last two solar cycles calculated using (21) for both ascending (top) and descending (bottom) orbits. The estimation performance is best at low latitudes where the azimuth-spread is large, but there is a strong dependency on longitude.

Fig. 10 shows the standard deviation and estimation bias for tracks along the prime meridian (top) and along the 116°E

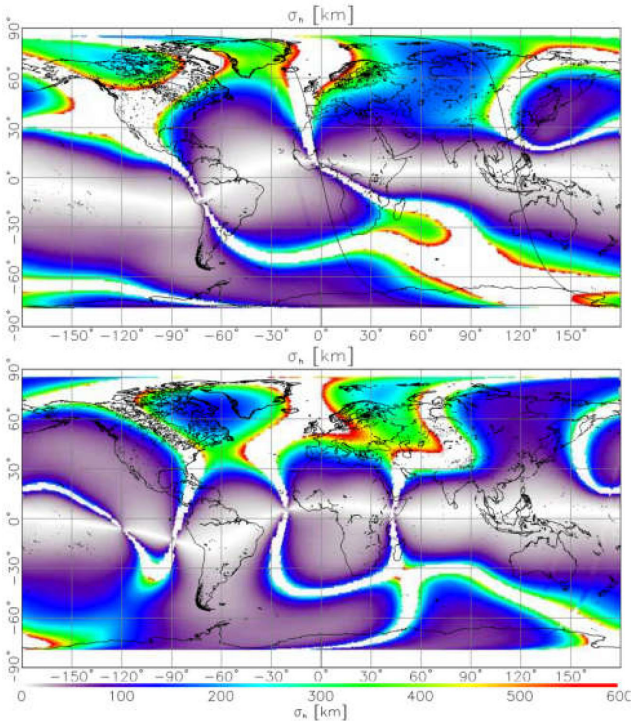

Fig. 9. Ionospheric height estimation accuracy maps using as reference the average TEC level of last two solar cycles. Top: ascending (midnight) and bottom: descending (noon) orbit.

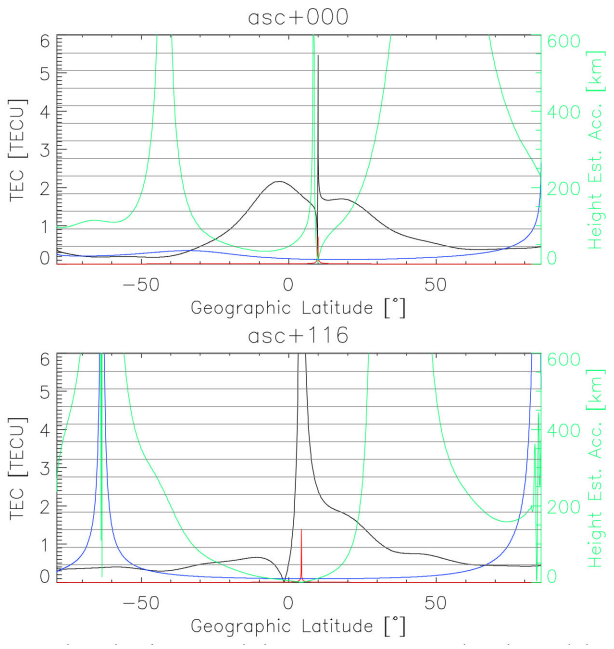

Fig. 10. Estimation uncertainties of TEC along (top) the prime and (bottom) 116°E meridians. The red line is TEC deviation from FR. The Black line is the TEC bias expected for 100 km ionospheric altitude change calculated for average TEC level of dawn-time passing orbit added with the TEC deviation. Blue line is the TEC estimation accuracy of proposed method. Green line is ionospheric height estimation accuracy and referring the y-axis on the right side. The gap between grey horizontal ticks corresponds to 2π ionospheric phase.

meridian (bottom). The red line indicates the standard deviation of TEC according to (16). The black line indicates the superposition of the standard deviation of TEC with the TEC bias induced by a 100 km ionospheric height estimation error at 300 km height for an average TEC level along a dawn-time ascending orbit (the same condition as the bottom of Fig. 8). The blue and the green lines indicate the standard deviation of TEC and ionospheric height estimation of the proposed method, respectively. The horizontal grey lines correspond to 2 π ionospheric phase cycles. The black line indicates that the ionospheric height uncertainty becomes the major uncertainty contribution in the FR-to-TEC conversion rather than the FR uncertainty itself (red line). Meanwhile, the proposed approach can apparently estimate TEC stable for a wide range of latitudes. However, the TEC estimation is coupled with the estimation of the ionospheric height (green line in Fig. 10). The range of reliable height estimation is restricted in a narrow band around the geomagnetic equator, and varies significantly with longitude (see Fig. 9).

Note that the height estimation accuracy for the 116°E meridian is good near the equator. And because the geometry of the 116°E meridian is almost identical with that of the ALOS-2 / PalSAR-2 dataset, the large fluctuation of height estimates in the southern scenes may have a different origin than the small height-spread.

C. Dynamic Scenario

The analysis up to now implicitly assumed that the TEC and the ionospheric height are constant within the estimation window (in this article, the whole scene extent). In this section, the perturbation induced by a TEC and/or height gradient within the estimation window is discussed.

The estimation of $d\Omega/d\beta$ under the variation of TEC and ionospheric height in the azimuth direction requires the expansion of (7)

$$\frac{d\Omega}{d\beta} = K\,\mathrm{TEC}\frac{d}{d\beta}\left(\vec{B}\cdot\hat{\kappa}\right) + K\frac{d\mathrm{TEC}}{d\beta}\vec{B}\cdot\hat{\kappa}_0$$
$$= K\mathrm{TEC}\vec{B}\cdot\hat{v}_0 + K\frac{dx}{d\beta}\left(\frac{d\mathrm{TEC}}{dx}\vec{B}\cdot\hat{\kappa}_0 + \mathrm{TEC}\frac{\partial\vec{B}\cdot\hat{\kappa}_0}{\partial h}\frac{dh}{dx}\right). \tag{22}$$

The second term on the right-hand side of (22) is the modification associated to the estimation geometry and the spatial variation of TEC and ionospheric height. Ideally the squint estimation, which is performed in the frequency domain, is not affected by the spatial variation of TEC and h. However, because of the finite scene extent the squinted geometry shifts the imaged extent of the ionosphere, so that the terms expressing the spatial variation appear in (22).

To compensate for the additional unknown term, the time domain FR gradient in azimuth (in the zero-Doppler geometry $\hat{\kappa}_0$), $d\Omega/dx$, is employed:

$$\frac{d\Omega}{dx} = K\frac{d\mathrm{TEC}}{dx}\vec{B}\cdot\hat{\kappa}_0 + K\cdot\mathrm{TEC}\left(\frac{\partial}{\partial x} + \frac{dh}{dx}\frac{\partial}{\partial h}\right)\left(\vec{B}\cdot\hat{\kappa}_0\right). \tag{23}$$

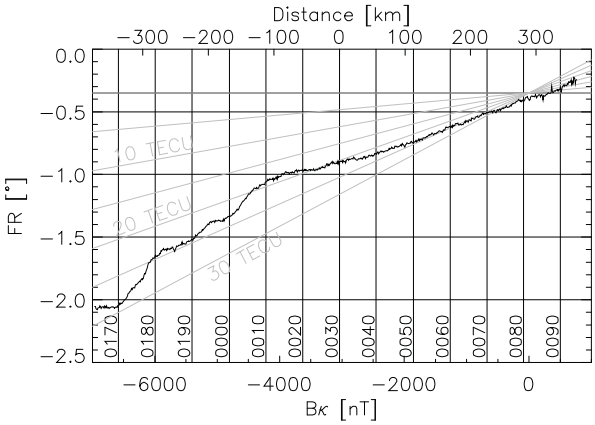

Fig. 11. FR profile showing finer structures than scene extent.

The first term on the right-hand side of (23) corresponds to the TEC variation, and the second describes the change of $\vec{B}\cdot\hat{\kappa}$ associated in azimuth and with ionospheric height. Substituting (23) into (22) follows:

$$\frac{d\Omega}{d\beta} = K\cdot\mathrm{TEC}\vec{B}\cdot\hat{v}_0 - h\left(\frac{d\Omega}{dx} - K\cdot\mathrm{TEC}\frac{\partial}{\partial x}\left(\vec{B}\cdot\hat{\kappa}_0\right)\right). \tag{24}$$

The negative relation between the squint and the azimuth position of the imaged ionosphere is accounted by using $\frac{dx}{d\beta} = -h$. The $\frac{\partial}{\partial x}(\vec{B}\cdot\hat{\kappa}_0)$ term can be estimated from the imaging geometry and the geomagnetic field, and is a function of the ionospheric height.

The TEC gradient compensation modifies the value of $d\Omega/d\beta$ and the height estimate in a sensitive way, as shown in Fig. 6. For a quantitative evaluation, (24) is multiplied by $d\beta/d(\vec{B}\cdot\hat{\kappa})$ to be analyzed in the "Bk–FR plot." Among the three terms on the right-hand side of (24), only $d\Omega/dx$ is associated to the TEC gradient. The maximum value of $d\Omega/dx$ across the 13 images is about 0.3°/70 km (the standard scene extent in azimuth). It corresponds to a 600 rad/T slope on the "Bk–FR plot" (as obtained after the multiplying with $d\beta/d(\vec{B}\cdot\hat{\kappa})$ and accounting for the 300 km altitude). This amount is substituted into (21) for the deviation of the slope σ_m on the Bk–FR plane. For the given geometry, the gradient of the y-intersection line shifts between 12.4×10^{-9} (at south) to 8.0×10^{-9} (at north) rad/m [$d\Omega_0/dh$ in (21)]. This leads, when substituted to (20), to an ionospheric height bias of about 300 km induced by the TEC gradient. However, this is not the final bias because the second term $h\cdot K\cdot\mathrm{TEC}\frac{\partial}{\partial x}(\vec{B}\cdot\hat{\kappa}_0)$ in (24) compensates for the FR change for a constant TEC reducing the final bias to about 150 km as indicated in Fig. 7.

Fig. 11 shows the FR profile of the whole sequence. There are two steps of rapid FR increase, one at 7170, and the other at 0000. As they are negative, the increase of FR is associated to the decrease of TEC. Although not very distinct, the TEC drop can be seen at the corresponding locations in Fig. 7. In Fig. 11, there are also finer (than the scene extent) structures visible, especially in the southern acquisitions. They are not captured in Fig. 7.

The slope on the "Bk–FR plot" is proportional to TEC [see (7)]. The lines originating from the point (0 nT, –0.35°) indicate the TEC level. The estimated TEC levels are in good agreement with the TEC estimates in Fig. 7. It is useful to remind here that 1 TECU corresponds to a slope of 154.67 rad/T in the "Bk–FR plot."

Using (3), (24) and the additional estimates of $d\Omega/dx$, it is possible now to estimate the TEC and height compensated with respect to TEC gradients within the estimation window. They are shown by the black lines in Fig. 7. The TEC estimates are not different from the original estimates (grey), while the height estimates at the lower levels are now more stable. The decrease of the height estimates at 7180 is due to the $d\Omega/dx$ estimation error associated to the low backscattering from the swap area (Fig. 3).

V. Conclusion

A new TEC and ionospheric height estimation approach has been proposed and evaluated. The approach relies on the dependency of FR (Ω) and its derivative with respect to squint angle β, (i.e., $d\Omega/d\beta$) on the TEC and ionospheric height. Using these two relations, the coupled estimation of both TEC and ionospheric height becomes possible. The approach has been demonstrated on a sequence of 13 ALOS-2 PALSAR-2 acquisitions transecting the Kalimantan Island, Indonesia along a 740 km strip that crosses where $\vec{B} \cdot \hat{\kappa} = 0$. Accordingly, the acquisition sequence crosses not only the point where $\vec{B} \cdot \hat{\kappa} = 0$ but also the point where the height-spread of $\vec{B} \cdot \hat{\kappa}$ (i.e., the variation of $\vec{B} \cdot \hat{\kappa}$ along the LOS) becomes minimum thus allowing to analyze the performance dependency on the imaging geometry.

The proposed approach performs best at a belt of some hundreds of kilometers width centered on the geomagnetic equator where $\vec{B} \cdot \hat{\kappa}$ is (close to) zero (known as the equatorial gap) where the conventional FR-to-TEC method fails because of the small $\vec{B} \cdot \hat{\kappa}_0$ values. This is an important missing element in the FR-based TEC estimation framework.

At the same time, the new approach allows the simultaneous estimation of the ionospheric height without requiring the presence of ionospheric irregularities. The estimated ionospheric height corresponds to the center of mass of the weighted electron density distribution associated to the measured FR (rather than to the height of the ionospheric irregularities obtained by means of parallax-based estimators relying on ionospheric irregularities).

With increasing latitude, the estimation accuracy of the ionospheric height becomes less and less reliable. The azimuth-spread of $\vec{B} \cdot \hat{\kappa}$ becomes small, and the values of $\vec{B} \cdot \hat{\kappa}$ is too far from the origin to estimate the line passing the origin correctly. A noteworthy effect is that the height estimation accuracy improves with increasing TEC level.

The spatial resolution of the FR estimates used in this article is very low: one FR estimate for the whole scene for each given squint (i.e., azimuth sub-band). Of course, the spatial resolution can be enhanced by reducing the FR estimation window, however, the window should still large enough to allow the robust Bk–FR slope estimation.

Furthermore, it has been shown that the spatial variation of TEC within the estimation window can bias the obtained TEC estimates. However, this bias can be compensated by using the time domain FR gradient in azimuth. The compensation performance depends on the surface cover type: at low-backscatter areas, the FR estimates in both time and frequency domain degrade.

A limitation of this article is the lack of detailed cross-validation ionospheric data. The TEC estimates could be compared only against the low-resolution GNSS TEC estimates, which are about 10 TECU higher. For the ionospheric height estimates, there are no reference data available.

Finally, the importance of accurate (polarimetric) system calibration has to be stressed. The theoretical description of the TEC and ionospheric height estimation method carried out in article is based on unbiased FR estimates. For the application to the ALOS-2 / PalSAR-2 datasets, however, the compensation of a residual FR bias, probably originating from residual polarimetric system distortion components, was required. The compensation was implemented in two steps: First, compensating a mean FR bias of 0.35° (to force zero FR when $\vec{B} \cdot \hat{\kappa} = 0$) and second by adding an offset of 0.001 radian to the FR estimates at positive Doppler frequencies (to compensate for the discontinuity of the of the FR estimates obtained in the transition from negatives to positives Doppler frequencies). In addition, the linear relation between FR and the squint angle β as predicted appears distorted at the high frequency end of the azimuth bandwidth probably also due to a residual polarimetric distortion component present at these higher (azimuth) frequencies.

Acknowledgment

ALOS-2 PALSAR-2 Level 1.1 data are provided by the Japan Aerospace Exploration Agency (JAXA) under the framework of Earth Observation Research Announcement. The ALOS-2/PALSAR-2 data used in this study are property of JAXA. We also acknowledge the critical and constructive reviews that strongly improved the paper.

References

[1] "Biomass: Report for mission selection," European Space Agency, ESAR communication Production Office, Noordwijk, the Netherlands, SP-1324/1, 2012. [Online]. Available: https://earth.esa.int/web/guest/document-library/browse-document-library/-/article/biomass-report-for-mission-selection-an-earth-explorer-to-observe-forest-biomass

[2] A. L. Gray, K. E. Mattar, and G. Sofko, "Influence of ionospheric electron density fluctuations on satellite radar interferometry," *Geophys. Res. Lett.*, vol. 27, no. 10, pp. 1450–1454, 2000.

[3] C. S. Carrano, K. M. Groves, and R. G. Craton, "Simulating the impacts of ionospheric scintillation on L-band SAR image formation," *Radio Sci.*, vol. 47, no. 4, Aug. 2012, Art. no. RS0L20.

[4] F. J. Meyer, K. Chotoo, S. D. Chotoo, B. D. Huxtable, and C. S. Carrano, "The influence of equatorial scintillation on L-band SAR image quality and phase," *IEEE Trans. Geosci. Remote Sens.*, vol. 54, no. 2, pp. 869–880, Feb. 2016.

[5] M. Shimada, Y. Muraki, and Y. Otsuka, "Discovery of anoumoulous stripes over the amazon by the PALSAR onboard ALOS satellite," in *Proc. IEEE Int. Geosci. Remote Sens. Symp.*, 2008, pp. II–387–II–390.

[6] D. P. Belcher, "Theoretical limits on SAR imposed by the ionosphere," *IER Radar, Sonar Navigation*, vol. 2, no. 6, pp. 435–448, Dec. 2008.

[7] F. J. Meyer, R. Bamler, N. Jakowsky, and T. Fritz, "The potential of low frequency SAR systems for mapping ionospheric TEC distributions," *IEEE Trans. Geosci. Remote Sens. Lett.*, vol. 3, no. 4, pp. 560–564, Oct. 2006.

[8] F. J. Meyer and J. B. Nicoll, "Prediction, detection and correction of faraday rotation in full-polarimetric L-band SAR data," *IEEE Trans. Geosci. Remote Sens.*, vol. 46, no. 10, pp. 3076–3086, Oct. 2008.
[9] S. R. Cloude, *Polarisation: Applications in Remote Sensing*. Oxford, U.K.: Oxford Univ. Press, 2010.
[10] S. H. Bickel and R. T. H. Bates, "Effects of magneto-ionic propagation on the polarization scattering matrix," *Proc. IEEE*, vol. 53, no. 8, pp. 1089–1901, Aug. 1965.
[11] P. A. Wright, S. Quegan, N. S. Wheadon, and C. D. Hall, "Faraday rotation effects on L-band spaceborne SAR data," *IEEE Trans. Geosci. Remote Sens.*, vol. 41, no. 12, pp. 2735–2744, Dec. 2003.
[12] X. Pi, A. Freeman, B. Chapman, P. Rosen, and Z. Li, "Imaging ionospheric inhomogeneities using spaceborne synthetic aperture radar," *J. Geophys. Res.*, vol. 116, Apr. 2011, Art. no. A04303.
[13] M. C. Kelley, *The Earth's Ionosphere: Plasma Physics and Electrodynamics*. San Francisco, CA, USA, Academic, 2009.
[14] W. S. Schreiner, S. V. Sokolovskiy, C. Rocken, and D. C. Hund, "Analysis and validation of GPS/MET radio occulation data in the ionosphere," *Radio Sci.*, vol. 34, no. 4, pp. 949–966, Jul./Aug. 1999.
[15] M. M. Hoque and N. Jakowski, "A new global model for the ionospheric F2 peak height for radio wave propagation," *Ann. Geophys.*, vol. 30, pp. 797–809, May 2012.
[16] J. S. Kim, K. P. Papathanassiou, R. Scheiber, and S. Quegan, "Correcting distortion of polarimetric SAR data induced by ionospheric scintillation," *IEEE Trans. Geosci. Remote Sens.*, vol. 53, no. 12, pp. 6319–6335, Dec. 2015.
[17] J. S. Kim and K. P. Papathanassiou, "On the separation of dynamic scattering and ionospheric effects in SAR data," in *Proc. POLinSAR*, 2015.
[18] J. S. Kim, H. Sato, and K. Papathanassiou, "Validation of ionospheric mapping by means of SAR through ground based radar measurements," in *Proc. 11th Eur. Conf. Synthetic Aperture Radar*, 2016, pp. 1–6.
[19] J. S. Kim, "Development of ionosphere estimation techniques for the correction of SAR data," Ph.D. dissertation, Dept. Civil, Environ. Geomatic Eng., ETH, Zürich, Switzerland, 2013.
[20] D. Turcotte and G. Schubert, *Geodynamics*. Cambridge, U.K.: Cambridge Univ. Press, 2014.
[21] E. Thebault *et al.*, "International geomagnetic reference field: The 12th generation," *Earth, Planets Space*, vol. 67, May 2015, Art. no. 79.
[22] J. S. Kim, K. P. Papathanassiou, H. Sato, and S. Quegan, "Detection and estimation of equatorial spread f scintillations using synthetic aperture radar," *IEEE Trans. Geosci. Remote Sens.*, vol. 55, no. 12, pp. 6713–6725, Dec. 2017.
[23] J. S. Kim and K. P. Papathanassiou, "Polarimetric calibration of spaceborne SAR data under faraday rotation by means of sub-bands analyses," in *Proc. CEOS Cal/Val Workshop*, 2019.
[24] K. P. Papathanassiou and J. S. Kim, "Polarimetric system calibration in the presence of faraday rotation," in *Proc. IEEE Int. Geosci. Remote Sens. Symp.*, 2017, pp. 2430–2433.
[25] "BIOMASS external calibration study report," European Space Agency, 2017.
[26] H. Lühr, S. Maus, M. Rother, and D. Cooke, "First in-situ observation of nighttime f region currents with the CHAMP satellite," *Geophys. Res. Lett.*, vol. 29, no. 10, May 2002, Art. no. 1489.
[27] International Service of Geomagnetic Indices, [Online]. Available: http://isgi.unistra.fr/
[28] S. Schaer, W. Gurtner, and J. Feltens, "IONEX: The IONosphere map exchange format version 1," in *Proc. IGS AC Workshop*, 1998, pp. 233–247.